Biology of Reproduction, 2021, 00(00), 1–13
doi:10.1093/biolre/ioab043
Research Article

Research Article

Anatomical and cellular heterogeneity in the mouse oviduct—its potential roles in reproduction and preimplantation development[†]

Keerthana Harwalkar[1,2], Matthew J. Ford[1,2], Katie Teng[1,2], Nobuko Yamanaka[1], Brenna Yang[1], Ingo Burtscher[3,4], Heiko Lickert[3,4,5,6] and Yojiro Yamanaka[1,2,*]

[1]Rosalind and Morris Goodman Cancer Research Centre, Montreal, Quebec, Canada, [2]Department of Human Genetics, McGill University, Montreal, Quebec, Canada, [3]Institute of Diabetes and Regeneration Research, Helmholtz Diabetes Center, Helmholtz Center Munich, Munich, Germany, [4]Institute of Stem Cell Research, Helmholtz Center, Munich, Germany, [5]German Centre for Diabetes Research (DZD), Munich, Germany and [6]Department of Medicine, Technical University of Munich, Munich, Germany

***Correspondence:** 1160 Pine Avenue West, rm419, Montreal, Quebec H3A 1A3, Canada.
Tel.: 514-398-8776; E-mail: yojiro.yamanaka@mcgill.ca

[†]**Grant Support:** This work was supported by Canadian Cancer Society (CCS) Innovation Grant (Haladner Memorial Foundation #704793), CCS innovation to Impact (i2I) Grant (#706320), and Cancer Research Society Operation Grant (#23237). KH was supported by Centre for Research in Reproductuion and Development (CRRD), Alexander McFee, and Rolande & Marcel Gosselin graduate studentships. MF was supported by Canderel, CRRD, and Fonds de recherche du Québec - Santé (FRQS) postdoc fellowships. KT was supported by McGill Integrated Cancer Research Training (MICRTP) and Canderel graduate studentships.

Received 24 August 2020; Revised 25 December 2020; Editorial Decision 3 March 2021; Accepted 4 March 2021

Abstract

The oviduct/fallopian tube is a tube-like structure that extends from the uterus to the ovary. It is an essential reproductive organ that provides an environment for internal fertilization and preimplantation development. However, our knowledge of its regional and cellular heterogeneity is still limited. Here, we examined the anatomical complexity of mouse oviducts using modern imaging techniques and fluorescence reporter lines. We found that there are consistent coiling patterns and turning points in the coiled mouse oviduct that serve as reliable landmarks for luminal morphological regionalities. We also found previously unrecognized anatomical structures in the isthmus and uterotubal junction, which likely play roles in reproduction. Furthermore, we demarcated the ampulla–isthmus junction as a distinct region. Taken together, the oviduct mucosal epithelium has highly diverse structures with distinct epithelial cell populations, reflecting its complex functions in reproduction.

Summary sentence: The mouse oviduct mucosal epithelium has highly diverse structures with 7 distinct epithelial cell populations, likely reflecting its complex functions in reproduction.

Graphical Abstract

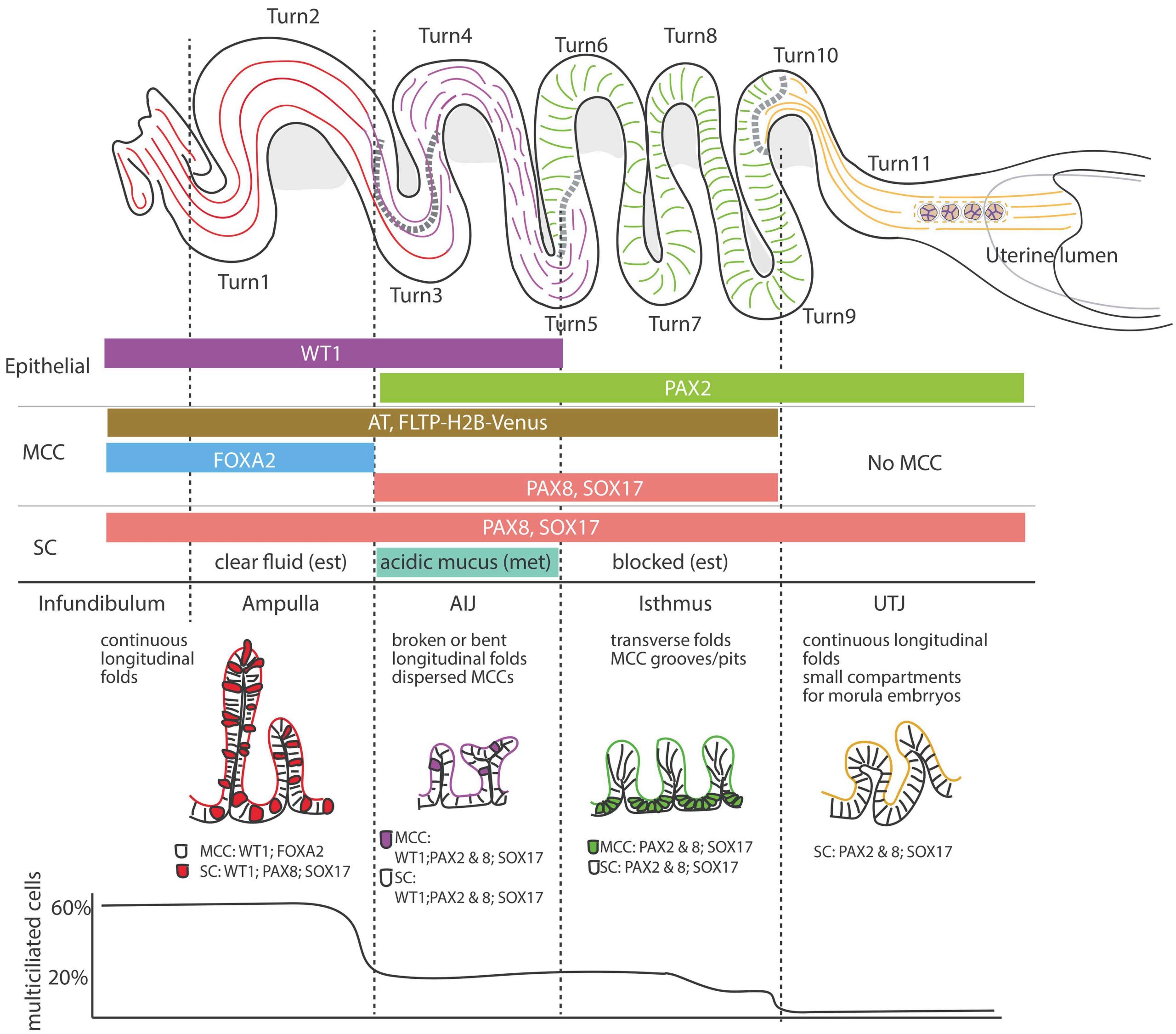

Key words: oviduct, fallopian tube, mucosal epithelium, mucosal folds, sperm reservoir, preimplantation embryo development.

Introduction

Mouse oviducts, called fallopian tubes (FTs) in humans, are a part of the female reproductive tract; they are tube-like structures that extend from the uterus to the ovary. This organ is essential for mammalian reproduction, including internal fertilization and preimplantation development. Sperm and oocytes enter from opposite ends of the oviduct to meet at a transiently distended region of the oviductal ampulla (AMP) for fertilization. After fertilization, preimplantation embryos travel down the oviduct lumen toward the uterus [1, 2]. They remain in the oviduct for relatively consistent period of time without direct physical contact between the embryos and oviductal mucosal epithelium due to the remaining presence of the oocyte zona pellucida, a proteinaceous shell that surrounds each embryo during its time in the oviduct [3]. The oviduct luminal environment is transiently modulated by the oviductal mucosal epithelium to accommodate sperm migration, fertilization, and preimplantation development [4–6]. Without this regulation, the oviduct luminal environment is too harsh for reproduction because it is primarily adjusted against bacterial infections [6]. On the other hand, if a preimplantation embryo does not properly traverse the tube, for example, due to an obstruction or constriction in the luminal space, this leads to ectopic pregnancy in humans [7]. This indicates that a proper spatiotemporal coordination between the oviduct and gamete/embryo movement is essential for successful pregnancy.

Although the oviduct is essential for reproduction, with a portion of human infertility cases being due to deficiencies in the oviduct [8], the complexity of mucosal fold patterns and cellular heterogeneity of the oviduct mucosal epithelium have not been fully explored. The pioneering work on the mouse oviduct [9] described intensive oviduct coiling and complex luminal morphology. Four regionalities are recognized in the mouse oviduct, from distal to proximal with point of reference as the uterus: the infundibulum (INF), AMP, isthmus (ISM), and uterotubal junction (UTJ). It has been generally thought that the oviductal mucosal epithelium consists of two cell types: multiciliated cells (MCCs) and nonciliated secretory cells (SCs), with the proportion of MCCs forming a descending gradient from the distal to proximal [10, 11]. However, in our parallel study, we identified that distal and proximal luminal epithelial cells are two distinct lineages from as early as E12.5 in the Mullerian duct, presenting with unique gene expression [12].

In this study, we revisit the oviduct using modern imaging techniques and mouse fluorescence reporter lines. Due to its intensive coiling, traditional 2D tissue sectioning methods have limitations in the analysis of 3D complexity. Through our careful 3D analysis, we recognized consistent coiling patterns between mice, with corresponding changes in luminal regional morphology. In addition, we identified previously unrecognized anatomical structures in the ISM and UTJ, likely playing roles in successful pregnancy. The AMP–ISM junction (AIJ) was a unique region different from the AMP and ISM in its MCC distribution pattern, mucosal fold morphology, transcription factor expression, and acidic mucin secretion. Our results revealed anatomical and cellular heterogeneity in the mouse oviduct mucosal epithelium, suggesting functional diversity in each morphologically distinct region.

Results

Consistent coiling patterns in mouse oviducts maintained by its attachment to the mesosalpinx

The mouse oviduct is a highly coiled tube that extends from the uterus to the ovary. This coiling makes precise regional comparison difficult in standard 2D tissue sectioning methods. The mesosalpinx, which connects the oviduct to the body wall, gathers inferior to the coils and stabilizes them. It is also connected to the ovarian bursa as well as the uterine mesometrium, which is further attached to the dorsal mesentery [9]. We carefully compared several female reproductive tracts ($n = 10$ oviducts) to examine if they have consistent coiling patterns (Figure 1A, Supplementary Figure S1). Although occasional contractions of the AMP and ISM myosalpinx [13] created variation, their coiling pattern appeared consistent. The coiling pattern of the left and right oviducts was mirror images of each other. When the left oviduct was placed with the ovary on top and the uterus at bottom, the AMP was always positioned to the left side and the ISM was positioned to the right side (Figure 1A).

Based on the reproducible coiling patterns, we numbered each turn from the distal end (Figure 1C and D). Turns 1–4 were highly consistent. Turn 4 was often positioned inferior to Turns 2 and 3. Turns 5–7 presented with more variation, likely due to ISM contractions, with Turn 5 frequently curled toward the deep position. This created additional Turns 4.5 and 5.5 (Figure 1D and E, Supplementary Figure S1). Turns 9–11 were again relatively consistent. Turn 11 was often located at the deep position of the coiled oviduct and connected to the uterus (Figure 1B–D, Supplementary Figure S1). When the oviduct was straightened, each turn was still recognizable and the mucosal fold patterns along the oviduct were visible under a dark field illumination of a dissecting microscope (Figure 1F). The turning positions were reliable landmarks for mucosal fold patterns along the mouse oviduct.

3D imaging reveals transition of epithelial fold patterns along the mouse oviduct

In order to investigate mucosal fold patterns and their transition along the oviduct, we undertook high-resolution 3D confocal imaging analysis after tissue clearing. The INF is a funnel-like structure located at the distal end of the oviduct, adjacent to the ovary [9]. The mucosal epithelium of the INF was everted at its opening, called the ostium (Figure 2A, D, and G), where the lumen of the oviduct communicates with that of the ovarian bursa, exposing mucosal epithelium to the inner space of the ovarian bursa (Supplementary Figure S2). At the ostium, almost every two exterior longitudinal folds merged into one mucosal fold and continued into the AMP (Figure 2E). The distal end of the INF was not blunt, but often beveled to fit the ostium along the ovarian surface (Supplementary Figure S2). In contrast to the circular smooth muscle layer noted in a transverse section, the exterior mucosal folds were not radially symmetric (Figure 2B and D, Supplementary Figure S3A), with one side forming an overhang (Figure 2D and F, Video 1). Exterior folds on the contralateral side of the overhang were shorter and laid flat against the smooth muscle layer (Figure 2B and F, Video 1). The mucosal epithelium lining these exterior folds was continuous with the epithelium-lined ligament that connected to the ovarian bursa and ovary (Figure 2F, Supplementary Figure S2 and S3A). The INF mucosal folds consisted of 12–18 longitudinal folds (Supplementary Figure S3A, Figure 2B; $n = 8$ oviducts). Every other mucosal fold was tall (80–184 μm), reaching the center area of the lumen, with a short fold roughly half the height (16–80 μm) between two tall ones (Figure 2B, Supplementary Figure S3A). Each fold has a thin layer of stromal cells underneath the epithelium, without smooth muscle cells. The smooth muscle layer is only at the circumference, framing the tube-like shape at the INF [9].

The longitudinal mucosal folds of the INF and AMP were continuous (Figure 2A). The AMP had 15–20 inner mucosal folds (Figure 2C, Supplementary Figure S3B; $n = 8$ oviducts). The number of folds reduced between Turn 3 and 4 (5–12 mucosal folds; Figure 2H–K, Supplementary Figure S3C and D; $n = 8$ oviducts). Between Turns 4 and 5.5, the longitudinal folds were not continuous but showed slit-like breaking points (Figure 2L, Supplementary Figure S4B–D). Toward the proximal end, the AIJ longitudinal folds were often bent and had frequent breakpoints, with multiple convolutions (Figure 2M, Supplementary Figure S4A–F). Around Turn 6, transverse mucosal folds of the ISM were observed (Figure 2N, Supplementary Figure S3E and F), creating furrows extending along the circumference, comparable with a bellows shape (Figure 2P). Around Turn 6–8, the distal ISM, its transverse mucosal folds were not perfectly aligned/parallel but often fused (Figure 2N). On the other hand, around Turn 8–9, the transverse mucosal folds of the proximal ISM were aligned and parallel (Figure 2O).

The transition from transverse mucosal folds of the ISM to the longitudinal mucosal folds of the UTJ was observed around Turn 10 (Figure 2Q, Supplementary Figure S3G). In this transition area, the isthmic transverse folds were on the anti-mesosalpinx side, whereas 1–2 longitudinal UTJ folds were located on the opposing mesosalpinx side (Figure 2Q and R). UTJ longitudinal folds were inserted into the uterine stroma, forming the intramural UTJ (Figure 2S–U,

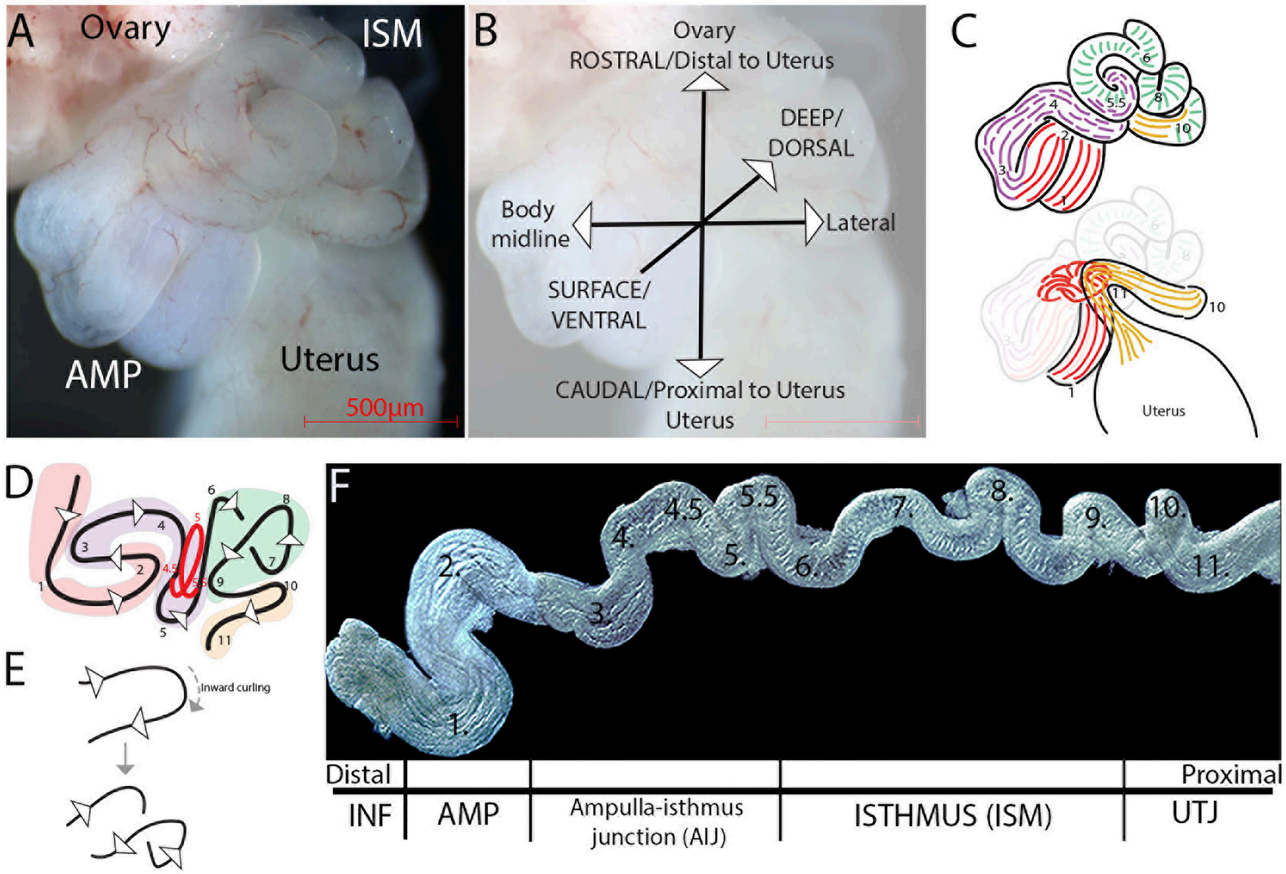

Figure 1. Consistent coiling pattern and turning points in the mouse oviduct. (A) Ventral view of the left mouse oviduct when the ovary–uterus axis is rostral–caudal, with AMP on the left and ISM on right-hand side of the image. (B) Axes representing the orientation of the coiled left oviduct. The surface/dorsal view to deep/ventral view is represented by a line directed into the paper. (C) Diagrams of the oviduct shown in A. Surface view (top) showing the body of the oviduct. Deep view (bottom) showing the INF and UTJ. The colors represent distinct mucosal fold morphologies: INF/AMP in red, AIJ in purple, ISM in green, and UTJ in yellow. (D) A simple illustration of the consistent coiling pattern and regionalities; 11 turns were reproducibly identified. Turn 5 was often curled toward the deep position (solid red line), creating Turns 4.5 and 5.5. The coiling pattern from Turn 5 to Turn 7 showed variation due to ISM contractile movement. Turns 1–3 and Turns 8–11 had consistent coiling pattern. (E) Coiling pattern in the ISM. The complex coiling pattern is created by a combination of turning and curling. (F) A stretched oviduct with mesosalpinx removed. Tiled images of the stretched oviduct were manually aligned. A plain black background was added; $N = 10$ oviducts.

Supplementary Figure S2). Interestingly, we found small luminal compartments within the intramural UTJ formed by breakpoints in the UTJ longitudinal folds (Supplementary Figure S4G–K, Figure 2T, Video 2). The intramural UTJ lumen communicated with the uterine lumen through the colliculus tubarius (Figure 2S, Video 2, Supplementary Figure S4G), as described previously [9, 14].

MCCs in the ISM are clustered at the trenches of transverse mucosal folds

It is thought that the proportion of MCCs forms a descending gradient from the distal end adjacent to the ovary [10, 11]. Since the mouse oviduct has complex mucosal folds and a highly coiled structure, it is important to perform 3D image analysis to capture the whole view of their distribution pattern. Using a *FLTP-H2B-Venus* (*Flattop-driven H2B-Venus* reporter) transgenic mouse line [15] for visualization of MCCs, we found that the distribution of FLTP-H2B-Venus+ve cells did not show a simple gradient, but a sharp reduction between Turns 2 and 3 (Figure 3A and B). A high proportion of FLTP-H2B-Venus+ve cells in the INF and AMP was observed (57.9 ± 3.57 and 55.4 ± 9.6%, respectively, mean ± SD; Figure 3G, Supplementary Figure S3A and B), with a relatively low proportion in the AIJ and ISM (ranging from 18 to 25%; Figure 3G, Supplementary Figure S3C–F). No FLTP-H2B-Venus+ve cells were found in the UTJ (Figure 3G, Supplementary Figure S3G).

In the INF and AMP, MCCs were uniformly distributed on the mucosal folds (Figure 3C and D, Supplementary Figure S3A and B). In the distal AIJ around Turn 3, MCCs were sparsely distributed (Figure 3E, Supplementary Figure S3C and S4A–D). Some MCCs in the proximal AIJ were located in the trenches of transverse mucosal folds (Figure 3F, Supplementary Figure S3D and S4E and F), similar to the ISM (Figure 3H–S), whereas others were sparsely distributed on the folds (Figure 3F, Supplementary Figure S3D and S4E and F). Although the location of MCCs changed progressively, there was no significant difference in the proportion of MCCs within the AIJ (17.99 ± 0.42% in distal compared with 21.67 ± 5.71% in proximal, Figure 3G).

In the ISM, interestingly, MCCs clustered in the trenches of the transverse folds (Figure 3H, Supplementary Figure S3E and F).

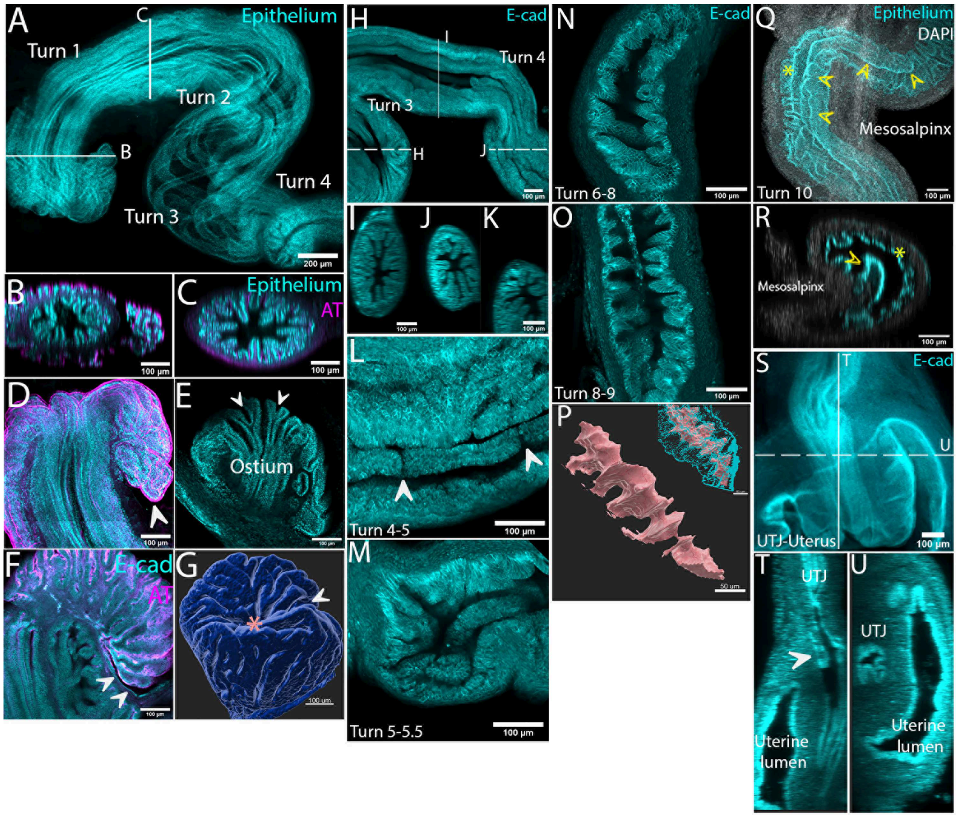

Figure 2. Distinct 3D luminal morphologies along the mouse oviduct. (A) The distal end of the oviduct from Turns 1–4, including the INF, AMP, and AIJ. Continuous, longitudinal folds extended from the INF into Turns 3–4. Sum slices projection of 90 optical sections. White lines indicate location of orthogonal views in (B) and (C). (B) XZ orthogonal view of the INF. (C) YZ orthogonal view of the AMP. Tall and short mucosal folds alternate along the circumference. (D) Exterior folds of the INF were continuous with the mucosal folds. The marginal edge of the exterior folds formed an overhang (white arrowhead). Maximum projection of 23 optical sections. (E) Two exterior folds merged into a single mucosal fold at the ostium (white arrowheads). (F) Intersection of overhanging and flattened exterior mucosal folds. Mucosal epithelium of exterior folds was connected to an epithelium-lined connective tissue (white arrowheads). (G) Surface rendered image of the INF. The exterior folds created a relatively wide flat surface leading to the ostium (pink asterisk). A slit opening towards the ovary (white arrow). (H) Continuous longitudinal folds from Turns 3 to 4 of the AIJ. White lines indicate the location of orthogonal views in I–K. (I) The area between Turns 2 and 3, (J) Turns 3 and 4, (K) Turns 4 and 5. A decrease of the number of longitudinal folds was noted. (L) The distal AIJ at Turns 4–5. Breakpoints in the longitudinal folds (white arrows). (M) The proximal AIJ at Turns 5–6. Short and bent longitudinal folds and luminal convolutions. (N) The distal ISM at Turns 6–8. Transverse mucosal folds were angled. (O) The proximal ISM at Turns 8–9. Aligned, parallel transverse mucosal folds. (P) Surface rendering of the bellows-shaped isthmic lumen. A merged image of the epithelial cell surface rendering and luminal surface rendering (inset). Scale bar = 50 µm. (Q) The transition between the ISM and UTJ around Turn 10. One longitudinal fold (yellow arrowheads) on the mesosalpinx side extended into the UTJ, with isthmic transverse folds on the anti-mesosalpinx side (yellow asterisk). (R) XZ orthogonal view in (Q). (S) The UTJ–uterus connection. The UTJ lumen, located within the uterine stroma, connected into the uterine lumen. Average projection of 115 optical sections. (T) Longitudinal orthogonal view in (S). Breakpoints in the longitudinal folds formed small compartments (white arrow). (U) Transverse view in (S). Intramural UTJ was at the mesosalpinx side of the uterine lumen. Epithelium: a combined signal of PAX8 and FLTP-H2B-Venus (used in A–E, Q, R; see Methods and Materials section); AT: acetylated tubulin; E-cad: E-cadherin; $N = 4$ mice. Scale bar = 100 µm, unless mentioned above.

Rosette arrangement of MCC clusters (Figure 3N and O) generated MCC grooves (Figure 3J and K) and pits (Figure 3L and M). All cilia were projected into one focal point within the clusters (Figure 3J–M), creating the stripe patterns of multicilia in the ISM (Figure 3I). The noted stripe patterns were very similar to the sperm distribution pattern shown in previous studies [14, 16, 17]. Although the trench localization of MCCs in both distal and proximal ISM did not change (Figure 3P–S), there was a significant decrease in the proportion of MCCs in the proximal ISM (distal 25.26 ± 4.45% and proximal 14.91 ± 5.02%; Figure 3G). The density of MCCs was lower in the proximal ISM (Figure 3P and Q) because the number of MCCs forming each cluster was smaller (Figure 3R and S).

Distinct subtypes of SCs and MCCs in distal and proximal regions in mice and marmosets

In a parallel study, we demonstrated that distal and proximal oviduct mucosal epithelial populations are two developmentally distinct lineages as early as the E12.5 Mullerian duct. Based on single-cell transcriptome analysis, we identified that WT1 and PAX2 are specific markers for the distal and proximal regions, respectively. Interestingly, PAX8 is a marker for SCs only in the distal region, but is expressed in both SCs and MCCs of the proximal oviduct epithelium [12] (Figure 4A–F, Supplementary Figure S5A and D).

We searched for other transcription factors differentially expressed in the two regions and identified SOX17 and FOXA2.

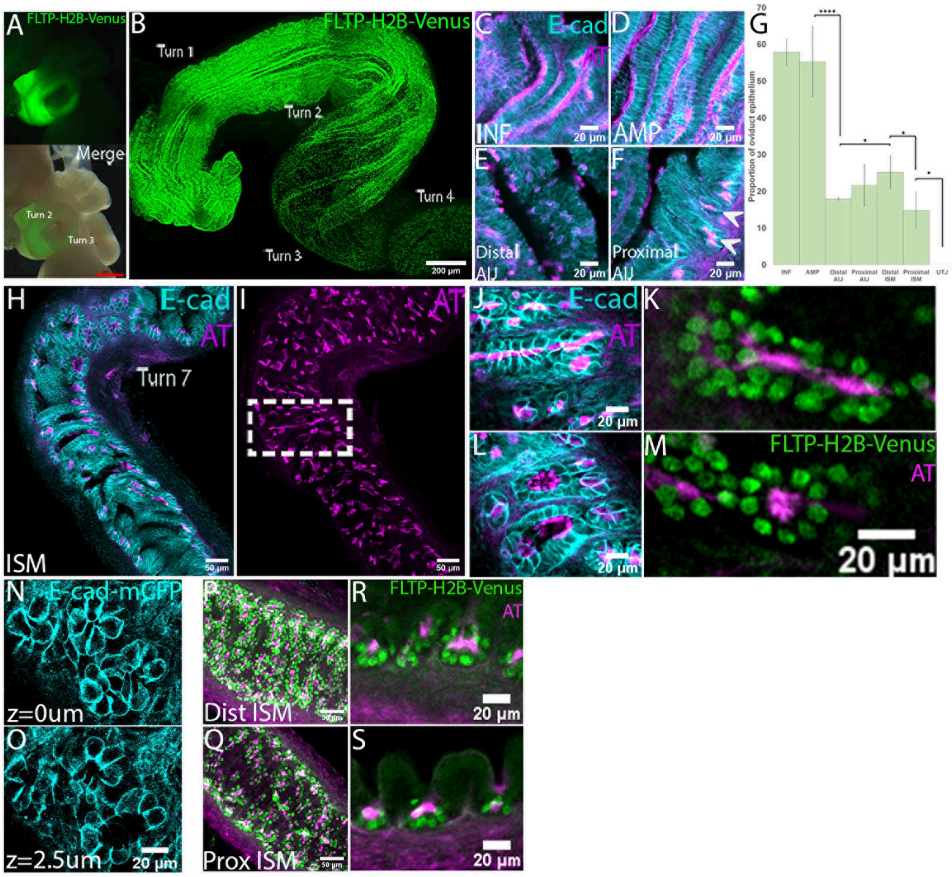

Figure 3. Distribution of multiciliated cells in the oviduct and unique multiciliated cell clusters in the ISM. (A) Unfixed oviduct of an FLTP-H2B-Venus female. Strong GFP signal in the INF and AMP. Scale bar = 500 μm. (B) Distribution of FLTP-H2B-Venus cells in the INF, AMP, and AIJ. A sharp reduction of H2B-Venus+ve cells between Turns 2 and 3. The same image series as Figure 2A. Maximum projection of 90 optical sections. Scale bar = 200 μm. (C–F) Distribution patterns of MCCs in the INF, AMP, and AIJ. (C, D) Uniform distribution of MCCs in the INF (C) and AMP (D). Cilia are evenly distributed on the apical surface. (E) MCCs are sparsely distributed in the epithelium of the distal AIJ. Cilia localization is not uniform but often limited at the periphery or center of the apical surface of MCCs. (F) MCCs in the proximal AIJ. They are located in the trenches (white arrowheads), similar to the ISM, but some are sparsely distributed on the folds. (G) Proportions of FLTP-H2B-Venus+ve MCCs along the oviduct. Regions of high (around 60% in INF/AMP), low (around 20% in AIJ/ISM), and absent (0% in UTJ) were recognized. $^{****}P < 0.0001$, $^{*}P < 0.05$. Error bars indicate standard deviation. Quantification was performed on transverse sections like those in Supplementary Figure S2A–G; $N = 8$ oviducts. (H–S) MCCs in the ISM. (H) A single optical section of the distal ISM. All MCCs are clustered in the trenches of the epithelial folds. (I) Maximum projection of acetylated tubulin staining from 41 optical sections. A groove pattern of the multicilia distribution, resembling the sperm distribution pattern [14, 16]. (J, K) A groove of MCC clusters. (L, M) Multiciliated cell pits. Cilia project to one focal point. (N, O) Live open-book preparations of the ISM isolated from *E-cadherin–mCFP* mice showing a rosette arrangement of cell clusters at the trenches, bottom of pits (N), close to mucosal surface (O). (P, Q) Difference in density of MCCs along the ISM. Maximum projections of FLTP-H2B-Venus and AT staining of the distal (P) and proximal (Q). Higher density of MCCs in the distal ISM than in the proximal ISM. (R, S) Longitudinal orthogonal views of distal (R) and proximal (S) isthmic transverse folds. More MCCs contribute to form single pits/grooves in the distal ISM. AT: acetylated tubulin; E-cad: E-cadherin. Scale bars = 20 μm/50 μm.

SOX17 and FOXA2 are both expressed in the uterine glandular epithelium but not in the uterine luminal epithelium [18, 19]. In contrast to their co-expression pattern in the uterine gland, their expression patterns in the oviduct were different. The expression of SOX17 in the oviduct was similar to PAX8 (Figure 4G–L, Supplementary Figure S5B and E). SOX17 was expressed in most PAX8+ve SCs of the INF and AMP (81.6 ± 15.12 and 72.2 ± 15.26% of PAX8+ve SCs, respectively, mean ± SD). Some double negative SCs (PAX8−ve; SOX17−ve) were also present (9.44 ± 3.16% in INF and 11.3 ± 4.76% in AMP) in the distal oviduct. On the other hand, SOX17 was expressed in both MCCs and SCs of the proximal regions (Figure 4H–L, Supplementary Figure S5B and E). Interestingly, FOXA2 was predominantly expressed in MCCs of the INF and AMP, but absent in the ISM–UTJ epithelium (Figure 4M–R, Supplementary Figure S5C and F).

We wondered whether these distal/proximal regionalities were evolutionarily conserved in other mammalian species, particularly in primates. The marmoset (*Callithrix jacchus*) is a nonhuman primate that has recently acquired a lot of attention because of its potential to be used as a genetic model for human diseases [20]. The adult marmoset female reproductive tract is anatomically similar to that of the human— uncoiled, bowed FTs extending from a single fused uterus [21]. At the distal end, finger-like projections called fimbriae, encompass the ovary (Supplementary Figure S6A and B, $N = 3$ marmosets). As expected, the proportion of MCCs was higher in the distal fimbriae and AMP (23.1 ± 5.99%) relative to the proximal ISM (6.67 ± 3.39%) (Figure 4S–V), whereas no MCCs were observed in the FT–uterus junction (0 ± 0%) (Figure 4W). In the mucosal epithelium of the fimbriae and AMP, PAX8 and SOX17 were expressed in SCs but not in MCCs (Figure 4X–Z, c–e), whereas

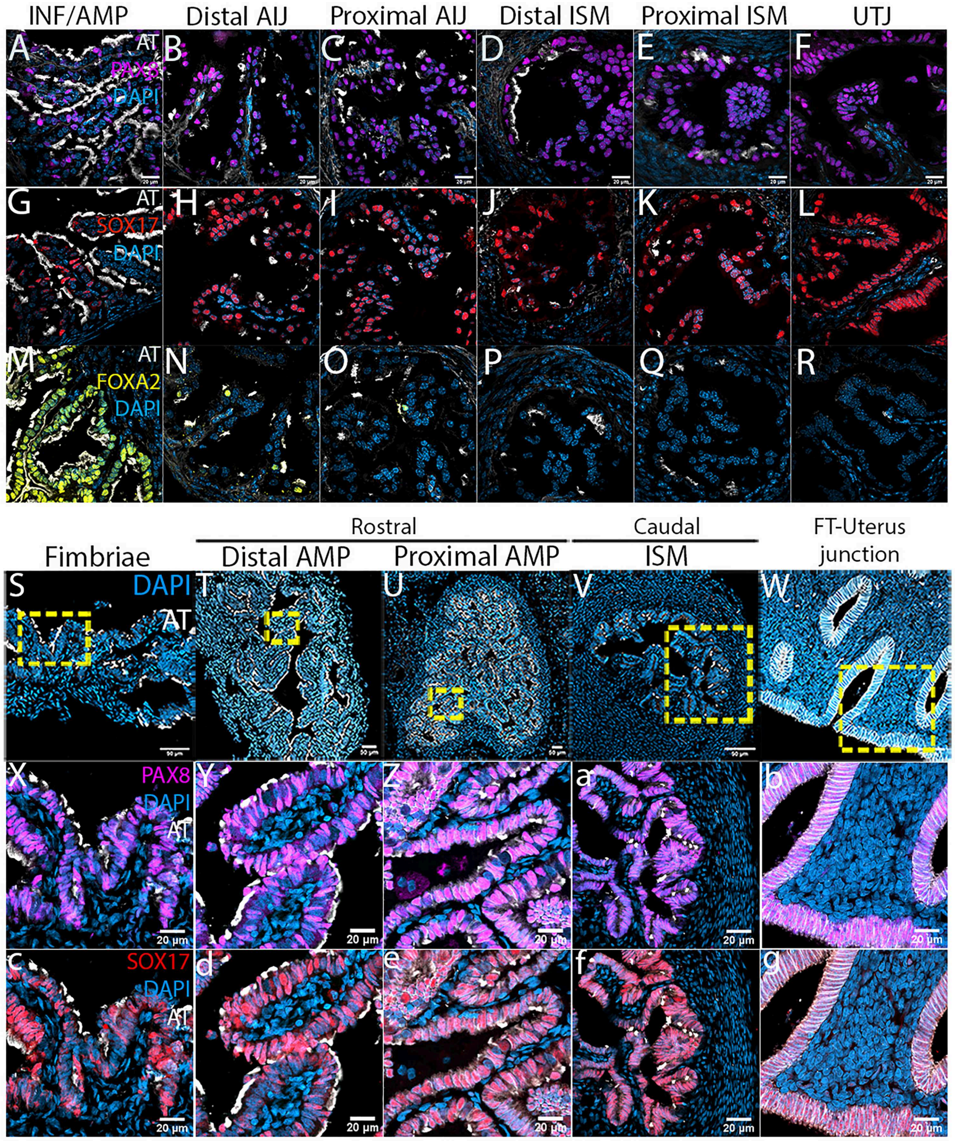

Figure 4. Distinct expression patterns of transcription factors in distal and proximal luminal epithelium in mice and marmosets. Expression patterns of PAX8 (A–F), SOX17 (G–L), and FOXA2 (M–R) in the mouse oviduct. (A, G, M) INF/AMP. (B, H, N) Distal AIJ. (C, I, O) Proximal AIJ. (D, J, P) Distal ISM. (E, K, Q) Proximal ISM. (F, L, R) UTJ. (A, G) PAX8 and SOX17 were expressed in nonciliated SCs in the INF and AMP. (B–F, H–L) PAX8 and SOX17 were expressed in all epithelial cells, both MCCs and nonciliated SCs. (M) FOXA2 was expressed in MCCs in the INF and AMP. (N–O) A very few MCCs in the AIJ expressed FOXA2. (P–R) No FOXA2-expressing cells in the ISM and UTJ; $N = 8$ oviducts. (S–W) Luminal morphology and MCC distribution in the marmoset fallopian tube. (S–U) The fimbriae and AMP showed complex luminal epithelial folds. (U) Dispersed AT+ve MCCs in the proximal AMP. (V) In the ISM, the lumen size is smaller, with thicker stromal and muscularis layer. Less complex folds. (W) The fallopian tube–uterus junction. The lumen size is larger. Smooth luminal surface lined with epithelium. Gland-like structures were noted, with no MCCs. (X–g) PAX8 and SOX17 expression pattern along the marmoset fallopian tube. (X–Z, c-e) PAX8 and SOX17 were expressed in nonciliated SCs in the INF and AMP. In the proximal AMP, the proportion of AT+ve MCCs were low, but they were PAX8−ve (Z) and SOX17−ve (e). (a, f) In the ISM, all epithelial cells were PAX8+ve (a) and SOX17+ve (f). (b, g) In the tube–uterine junction, all epithelial cells were PAX8+ve (b) and SOX17+ve (g), including gland-like structures. AT: acetylated tubulin; $N = 3$ marmosets. Scale bar = 20 μm.

in the ISM, both PAX8 and SOX17 were expressed in SCs and MCCs, similar to mice (Figure 4a and f). All epithelial cells in the FT–uterus junction expressed PAX8 and SOX17 (Figure 4b and g). These results indicate that distinct epithelial populations in the distal/proximal regions of the FT epithelium were evolutionarily conserved between mice and primates.

A sharp boundary of distal and proximal cell populations between Turns 2 and 3

A sharp reduction in the proportion of MCCs was observed between Turns 2 and 3 (Figure 3A and B). We found that the change in distribution pattern of PAX8+ve cells was complementary to the change in distribution pattern of FLTP-H2B-Venus+ve MCCs

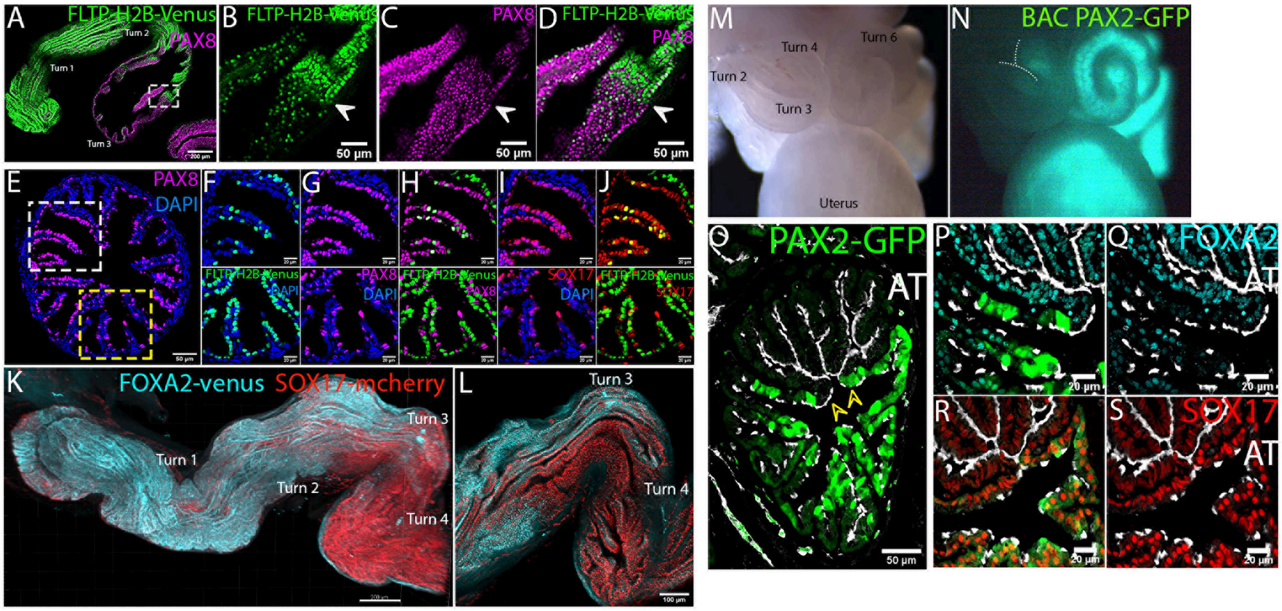

Figure 5. Sharp boundary of distal and proximal epithelial populations in the AIJ. (A–D) The sudden reduction of FLTP-H2B-Venus+ve cells coincides with the expression of PAX8 in both MCCs and SCs. Scale bar = 200 µm. (B) A boundary of the high proportion of FLTP-H2B-Venus+ve cells in the distal epithelium with the low proportion of FLTP-H2B-Venus+ve cells in the proximal epithelium. (C) A boundary of the distal epithelium where PAX8 was predominantly expressed in SCs with the proximal epithelium comprising MCCs and SCs that both express PAX8. (D) These two boundaries coincide (white arrowheads). Scale bars = 50 µm. (E) A transverse section of the boundary area. The folds with uniform PAX8+ve cells (white dotted box) and the folds with dispersed PAX8+ve cells (yellow dotted box). Scale bar = 50 µm. (F–H) (top panels) The folds with uniform PAX8+ve cells showed dispersed FLTP-H2B-Venus+ve cells. PAX8 and FLTP-H2B-Venus are co-expressed. (Bottom panels) The folds with dispersed PAX8+ve cells have high proportion of FLTP-H2B-Venus+ve cells. PAX8 and FLTP-H2B-Venus are mutually exclusive. Scale bar = 20 µm. (I, J) SOX17 expression is identical to PAX8. (K) 3D distribution pattern of FOXA2-venus and SOX17-mcherry cells. Their boundary of distinct distal/proximal distribution patterns between Turns 2 and 3. Maximum projection. Scale bar = 200 µm. (L) Single optical section. The proximal epithelium with uniform SOX17+ve cells extended distally on the mesosalpinx side, the inner side of Turn 3, forming a beveled boundary; $N = 4$ mice. Scale bar = 100 µm. (M, N) Proximally restricted *Pax2*-GFP expression. GFP expression boundary around Turns 2–3. (O) Transverse section showing the separate distribution of *Pax2*-GFP+ve and GFP−ve cells. A couple of folds show GFP+ve cells on one side and GFP−ve cells in the other side of the fold (yellow arrowheads). The GFP+ve and GFP−ve epithelia opposed at the ridge of the fold. The GFP+ve epithelium had fewer MCCs. Scale bar = 50 µm. (P, Q) Low proportion of FOXA2+ve cells in the *Pax2*-GFP+ve epithelium. (R, S) Uniform expression of SOX17 in *Pax2*-GFP+ve epithelium. AT: acetylated tubulin; $N = 4$ mice. Scale bar = 20 µm.

(Figure 5A–H). The distal epithelium with high proportion of FLTP-H2B-Venus+ve MCCs showed low proportion of PAX8+ve SCs, whereas the proximal epithelium with low proportion of FLTP-H2B-Venus+ve MCCs showed uniform PAX8+ve cells (both MCCs and SCs) with a straight boundary (Figure 5B–D). In a transverse section, the folds with dispersed PAX8+ve cells showed high proportion of FLTP-H2B-Venus+ve cells, with their expression being mutually exclusive. On the other hand, the folds with uniform PAX8+ve cells showed dispersed FLTP-H2B-Venus+ve cells where they were co-expressed (Figure 5E–H). The distribution pattern of SOX17 was identical to that of PAX8+ve cells (Figure 5I and J). This boundary was always beveled, with the proximal population extending distally on the mesosalpinx side, located on the inner side of Turns 2–3 (Figure 5A, K, and L).

In our parallel study, we demonstrated that PAX2 expression is restricted to the proximal oviduct mucosal epithelial cells [12]. Using BAC paired box 2 gene (*Pax2*)-green fluorescent protein (*GFP*) mice [22], the boundary of the proximal *Pax2*-GFP+ve and distal *Pax2*-GFP−ve cells was visualized between Turns 2 and 3, coinciding with the other boundaries above (Figure 5M and N). In a transverse section of the boundary, we observed localization of distal *Pax2*-GFP−ve cells on the anti-mesosalpinx side, and proximal *Pax2*-GFP+ve cells on the mesosalpinx side (Figure 5O). A couple of folds at this boundary showed *Pax2*-GFP+ve cells on one side and *Pax2*-GFP−ve cells on the other side, opposed at the ridge of the same fold. The boundary of the distinct distribution patterns of FOXA2+ve cells (Figure 5P and Q) and SOX17+ve cells (Figure 5R and S) also coincided. Therefore, all boundaries of the distinct distal/proximal expression patterns of PAX8, FOXA2, SOX17, and PAX2 coincided with the distinct distal/proximal distribution pattern of MCCs between Turns 2 and 3. This supports the conclusion of our parallel study that the distal/proximal epithelial cells are separately maintained distinct lineages [12].

Proximally extended WT1 expression generates a distinct population in the distal PAX2+ve cells of the AIJ

WT1 is uniquely expressed in the distal luminal epithelial cells [12] (Figure 6A–F). Interestingly, however, the boundary of WT1+ve and WT1−ve cells was different from the sharp boundary mentioned above between Turns 2 and 3, it was shifted proximally to around Turn 6 (Figure 6G and J). WT1 was not restricted in the *Pax2*-GFP−ve distal cell population, but was also expressed in the *Pax2*-GFP+ve cell population of the AIJ (Figure 6B, C, and G–I). The proportion of WT1+ve cells gradually decreased within the AIJ (Figure 6M, Supplementary Figure S7; 89.5 ± 15.12 and 52.5 ± 9.8% in distal and proximal

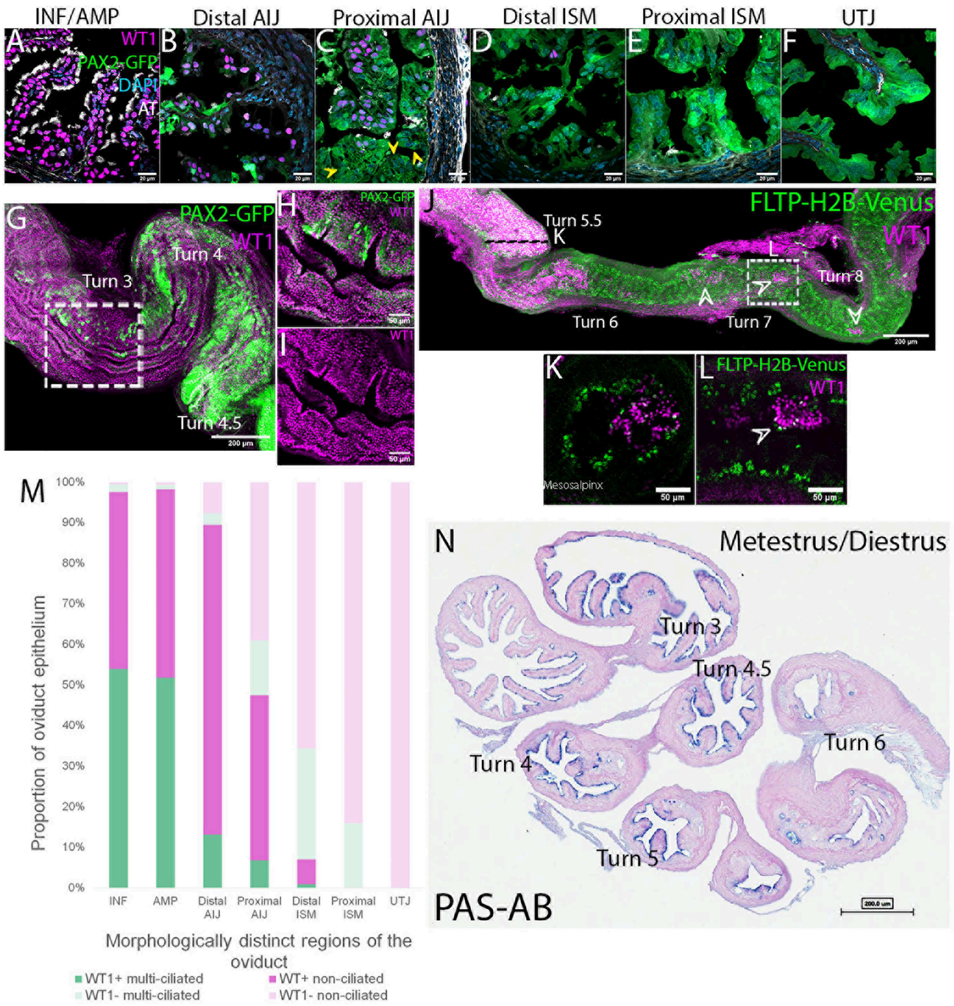

Figure 6. Boundary of WT1 expression extends into the proximal AIJ. (A–F) Distribution of WT1+ve and *Pax2*-GFP+ve cells in the oviduct epithelium. (A) INF/AMP. Uniform WT1+ve cells with no *Pax2*-GFP expression in the epithelium. (B, C) Distal and proximal AIJ. Co-expression of WT1 and *Pax2*-GFP. Some *Pax2*-GFP+ve cells are WT1−ve in the proximal AIJ (yellow arrowheads). (D) Distal ISM. (E) Proximal ISM. (F) UTJ. Scale bar = 20 µm. (G) WT1 expression extended into the proximal *Pax2*-GFP+ve population. Scale bar = 200 µm. (H, I) WT1 and PAX2 were co-expressed, but the level of WT1 was lower in the *Pax2*-GFP+ve cells; *N* = 4 oviducts. Scale bar = 50 µm. (J) WT1 expression boundary was located around Turn 6 with a few patches of WT1+ve cells in the distal ISM (white arrows). Scale bar = 200 µm. (K) Orthogonal view marked as the black dotted line in (J). WT1+ve cells were distributed on the folds on the anti-mesosalpinx side. The opposing mesosalpinx side had FLTP-H2B-Venus+ve cells in the trenches of transverse folds. They were not co-expressed. (L) Single optical section of the area indicated by a white dotted box in (J). Patches of coherent WT1+ve cells on the folds. WT1+ve cells were FLTP-H2B-Venus−ve. Scale bar = 50 µm. (M) Proportions of WT1+ve cells along the oviduct epithelium. Quantification was performed on transverse sections like A–F. (N) PAS–AB staining of the mouse oviduct during metestrus/diestrus. Dark Alcian blue staining was noted in only the AIJ epithelium. AT: acetylated tubulin.

AIJ, respectively). Interestingly, in the proximal AIJ between Turns 5 and 5.5, WT1+ve cells were predominantly nonciliated SCs, lining the short/broken longitudinal folds located on the anti-mesosalpinx side (Figure 3F and 6K and M). On the mesosalpinx side, where ISM-like transverse folds were observed, WT1+ve cells were absent from transverse folds (Figure 6C and K). Similar to the other two boundaries of AMP–AIJ and ISM–UTJ, the AIJ–ISM boundary was also beveled; the proximal WT1−ve isthmic transverse folds extended distally on the mesosalpinx side to the area of WT1+ve short/broken longitudinal folds. No WT1+ve cells were found in the proximal ISM and UTJ (6.97 ± 2.6 and 0 ± 0% in distal to proximal ISM, respectively; Figure 6D–F and M); however, we observed three to four patches of WT1+ve cells beyond the AIJ–ISM boundary in the distal ISM (Figure 6J and L).

Periodic acid–Schiff–Alcian blue (PAS–AB) staining is a common staining method to visualize neutral–acid mucin secretion from mucosal epithelia. When we stained the oviduct with PAS–AB staining, dense AB staining, indicating acid mucus secretion, was observed only in the AIJ epithelium at metestrus/diestrus, whereas no staining was noted in the AMP and ISM (Figure 6N; $N = 3$ mice). At estrus, no AB staining was observed in the oviduct, whereas some PAS staining, indicating neutral mucus secretion, was detected in the uterine glands (Supplementary Figure S8).

Taken together, our results indicated that the AIJ is different from the AMP and ISM in mucosal fold morphology (i.e., longitudinal with breakpoints), MCC distribution (i.e., sparse/dispersed), WT1 expression in the PAX2+ve population, and secretion regulation.

Oocytes and preimplantation embryos travel along the oviduct during fertilization and preimplantation development

It is known that fertilization takes place in the AMP [17, 23]. However, it is still unknown how the oocyte and sperm entering from the opposite ends of the oviduct can meet consistently at the AMP. Following ovulation, the AMP was swollen and filled with a clear serous fluid (Figure 7A and B). The oocyte–cumulus complexes were located around Turn 2, within the AMP (Figure 7B and C), encompassing the boundary of the two distal and proximal epithelial populations, as visualized by the sudden decrease in MCC proportion (Figure 7D). Interestingly, the swollen AMP maintained its shape even after the oviduct was detached from the uterus and the ovary, suggesting that both ends of the AMP were closed with no fluid leakage (Figure 7B). We found that both ends of the swollen AMP appeared physically constricted to close the lumen (Figure 7E). Indeed, when we injected trypan blue solution into the swollen AMP using a micropipette, the solution easily diffused into the AMP lumen, but entered neither the AIJ nor the ovarian bursa (Figure 7F and G; $N = 3$ mice). In contrast, when we tried to inject into the ISM of an estrus stage oviduct, a very small amount of the dye solution could be injected, the solution did not distribute in either direction within the ISM luminal space (Figure 7F and H, Supplementary Figure S9A and B). This suggests that the proximal region of the oviduct was sealed, possibly due to physical constriction, blocking any fluid flow and oocyte movement into the ISM.

Although the oviduct is known to be the place where preimplantation development occurs [1, 2], it is unknown whether the embryos are free floating in the oviduct lumen or they are located in a specific region of the oviduct. By 0.75 dpc, zygotes moved into the AIJ (Figure 7I and J). At 1.5 dpc, two-cell stage embryos were found in the ISM (Figure 7K and L), appearing floating in the lumen (Supplementary Figure S9C and D) with occasional ISM contractions. Interestingly, at 2.5 dpc, we found morula embryos in the UTJ (Figure 7M–O). The embryos formed a queue within the compartments found at the oviduct–uterus junction (Figure 2N and O).

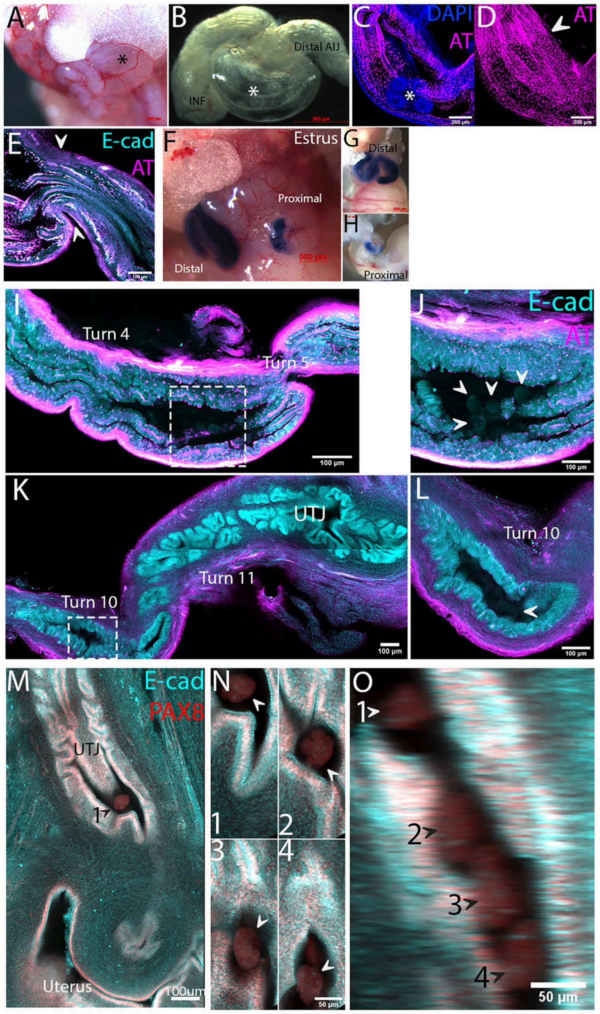

Figure 7. Preimplantation embryo travel in oviduct luminal space. (A) Prominent swollen AMP after ovulation (black asterisk). (B) A swollen AMP after dissection. Several oocyte–cumulous complexes are visible (white asterisk). Scale bar = 500 µm. (C) A swollen AMP containing 0.5 dpc embryos (white asterisk). Single optical section. (D) Maximum projection of AT staining of (C). The boundary of the distal/proximal populations (white arrow). Scale bar = 200 µm. (E) Single optical section showing the AIJ side of a swollen AMP. The lumen was closed by lumen constriction (white arrows). Scale bar = 100 µm. (F–H) Injection of trypan blue solution. (G) In the AMP and INF, trypan blue solution spread evenly, but did not into the AIJ or the ovarian bursa. (H) In the ISM, only a small amount of trypan blue solution could be injected. The blue dye did not spread but stayed at the injection site. (I) 0.75 dpc one-cell stage embryos in the AIJ around Turn 5. Characteristic broken longitudinal folds are observed, with sparsely distributed MCCs. Four zygotes are in the area marked with a dotted box. (J) Higher magnification of the area marked in (I). Floating zygotes (white arrowheads). This suggests that the AIJ was no longer sealed in this area by this time point. (K) 1.5 dpc. A two-cell stage embryo in the proximal ISM around Turn 10. A two-cell embryo is in the area marked in a dotted box. (L) Higher magnification of the area marked in (K). A two-cell embryo (white arrowhead). Scale bar = 100 µm. (M–O) 2.5 dpc. (M) Compartments were located at the junction of the oviduct and uterus. The first embryo and uterine lumen are shown (black arrow, numbered 1). Scale bar = 100 µm. (N) Four embryos (white arrows) located at different z-positions along the UTJ. (P) YZ orthogonal view. Four morula embryos formed a queue (white/black arrows, numbered 1–4). AT: acetylated tubulin; E-cad: E-cadherin; $N = 3$ mice. Scale bar = 50 µm.

Discussion

The oviduct is an essential organ for reproduction in mammals; however, its anatomical complexity and cellular heterogeneity have not been fully appreciated. Using modern imaging techniques and mouse fluorescence reporter lines, we made four major findings as follows (Figure 8): (1) AIJ is a distinct region from AMP and ISM. Thus, the oviduct consists of five regions: INF, AMP, AIJ, ISM, and UTJ; (2) INF/AMP, AIJ, and ISM have a unique pair of SCs and MCCs; (3) MCC clusters in the ISM form unique pits/groove structures at the trenches of transverse mucosal folds; and (4) E2.5 morula embryos are located in small compartments within the UTJ. In addition, we showed that consistent turning points in the mouse oviduct were associated with distinct luminal morphologies and epithelial populations. Many previous studies incorrectly compare different regions of the oviduct in traditional 2D sections due to lack of landmarks for the coiled oviduct. Our study described these turning points as reliable landmarks for precise description and comparison.

In the distal region, the primary role of MCCs is to support movement of the cumulus oocyte complex [24]. On the other hand, the role of MCCs in the ISM is unknown. Since multicilia of clustered

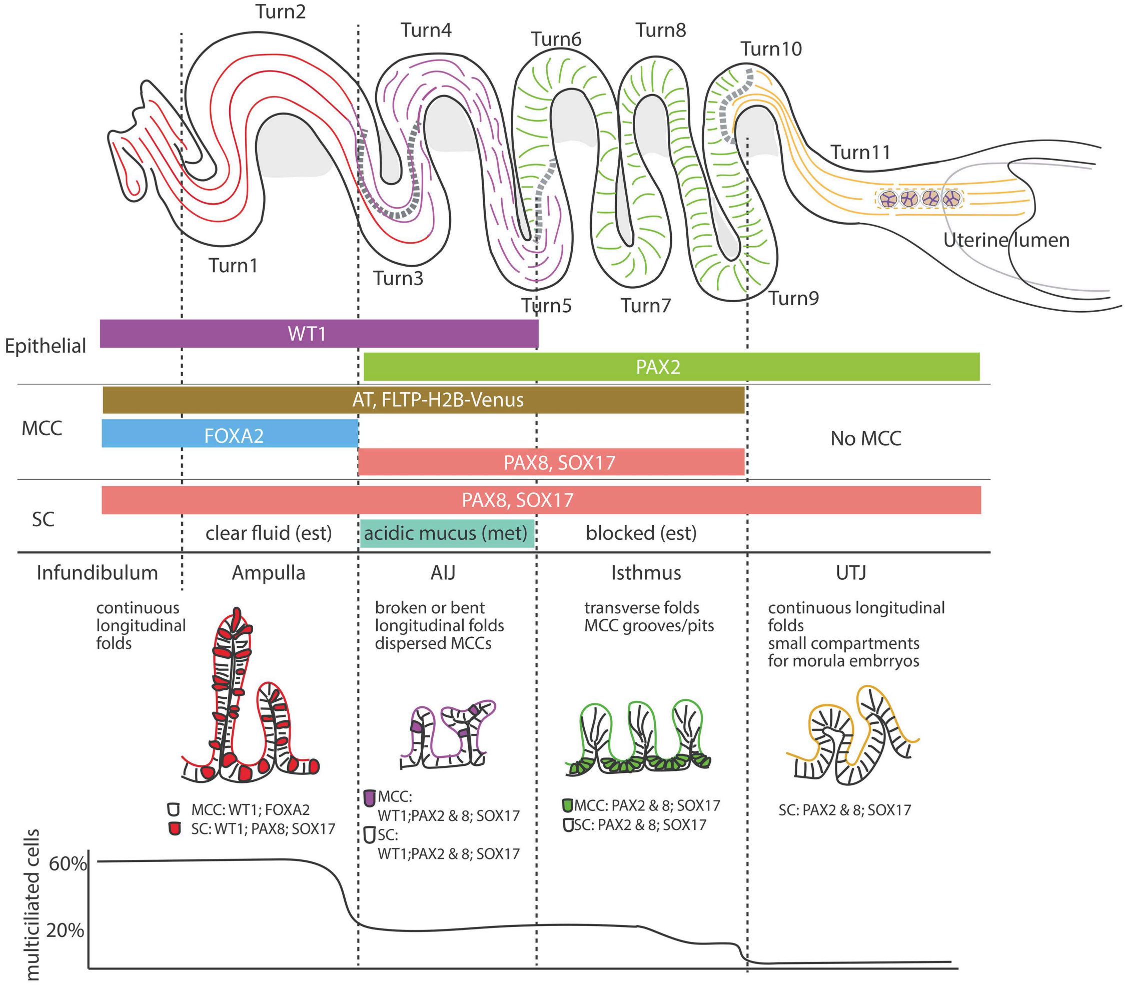

Figure 8. Model of anatomical and cellular heterogeneity of the oviductal luminal epithelium. Anatomical and cellular heterogeneity of the oviductal luminal epithelium. Turning points are linked with luminal morphological transitions. Five distinct regionalities, INF, AMP, AIJ, ISM, and UTJ, can be defined by luminal epithelial fold morphology, MCC distribution pattern, transcriptional factor expression pattern, and secretion. The INF/AMP, AIJ, and UTJ mucosal fold representations are that of transverse sections; however, the ISM mucosal fold representation is that of a longitudinal section. The distribution of MCCs did not form a gradient, but had three distinct proportions: high (INF/AMP), low (AIJ/ISM), and none (UTJ). Small compartments for morula embryos in the UTJ are also shown.

MCCs in the ISM project to the inside of pit/groove structures at the trenches of transverse mucosal folds, it is not clear if they can create a fluid flow in the luminal space to support preimplantation embryo movement. Interestingly, the stripe pattern of multicilia in the ISM is reminiscent of the immobilized sperm localization pattern [14, 16]. Furthermore, scanning electron microscopic studies of bull sperm indicate attachment of uncapacitated sperm to MCCs of the oviduct [25]. Studies in various species including mice allude to the presence of sperm attachment sites in the ISM, usually called sperm reservoirs [17, 26–30]. In addition, the gene expression pattern of ISM MCCs is different from that of INF/AMP MCCs [12], suggesting functional differences of MCCs in each region. The MCC clusters we identified in the ISM could function as sperm reservoirs, playing important roles in sperm viability, hyperactivation, and capacitation [26, 30].

Classic transmission electron microscopic studies in various mammalian species suggest that the distal and proximal oviduct epithelial cells have distinct secretary functions [31–35]. High to moderate electron-dense secretory granules in the INF and AMP suggest proteinaceous, serous secretion. Predominantly low electron-dense secretory granules suggest mucus-containing secretory granules in the ISM [31, 32, 35]. Our results were consistent with these classic observations. In the distal region, a clear serous fluid was observed in the swollen, estrus stage AMP. Interestingly, acid mucus secretion was observed in the AIJ predominantly at metestrus. It is recognized that various secretion molecules like antibacterial and fungal peptides are also secreted from the oviductal mucosal epithelial cells [4–6, 36]. How these secretions are regulated during the estrous cycle will be very important to understand gynecological diseases and infertility.

We identified that a sharp boundary of the distal PAX2−ve and proximal PAX2+ve populations was located between Turns 2 and 3. Interestingly, the boundary of WT1 expression did not coincide with this boundary, but was shifted proximally. This created a unique cell population of the AIJ that expressed WT1 in the proximal PAX2+ve population (Figure 8A). The unique AIJ mucosal fold morphology is briefly reported [4, 9, 37]. In addition to WT1/PAX2 expression, we found three other unique characteristics of the AIJ different from the AMP and ISM. First, multiple breakpoints and convolutions of AIJ longitudinal folds, in contrast to continuous longitudinal folds in the AMP and transverse folds in the ISM. Second, sparse distribution of PAX8+ve MCCs on the AIJ folds, in contrast to the uniform distribution of PAX8−ve MCCs on the AMP folds and the MCC pits/grooves in the ISM. Third, AIJ-specific acid mucin secretion indicated by Alcian blue staining at metestrus/diestrus, in contrast to no staining in the AMP and ISM. Taken together, we propose that the AIJ is a unique region different from the AMP and ISM, with distinct functions and unique gene expression.

Mouse preimplantation embryos stay in the oviduct for 3 days before implanting into the uterine lining [1, 2]; however, the location of embryos was unknown. We found that by E2.5 around the eight-cell stage, the embryos moved into previously unrecognized compartments of the UTJ, where the oviduct inserts into the uterus. In contrast to earlier stages where the embryos appeared to be floating in the ISM, E2.5 embryos formed a queue in the UTJ. It will be very interesting to determine what controls the timing of embryo entry into the uterus.

The intimate relationship between the oviduct epithelial cells and gametes/preimplantation embryos is essential for successful pregnancy. Our work provides a foundation to understand the oviduct luminal environment and homeostasis in reproduction.

Methods and materials

Animals

All animal work was performed in accordance with institutional guidelines and was approved by the Faculty of Medicine Animal Care Committee (AUP #7843); it was undertaken at the Goodman Cancer Research Centre animal facility. *Pax2-GFP Bac* [22] mice were kindly provided by Dr. Maxime Bouchard (McGill). *Fltp-H2B-Venus* [15], *FoxA2-venus* [38], *Sox17-mCherry* mice [39] mice were generated by Dr. Heiko Lickert and Dr. Ingo Burtscher (IDR Munich, Germany). *E-cadherin-mCFP* mice (monomeric cyan fluorescent protein fused to endogenous cadherin 1 protein ; B6.129P2(Cg)-Cdh1tm1Cle/J) were obtained from JAX. Adult mice used in this study were 2–4 months of age; oviducts were collected at random estrous stages. Where required, estrous stages were analyzed using vaginal smears stained with crystal violet [40]. Necropsy specimens of adult female marmoset reproductive tracts were kindly provided by Dr. Jim Gourdon (CMARC, McGill) and Dr. Keith Murai (McGill).

Whole-mount immunostaining, tissue clearing, and 3D confocal imaging

After euthanasia, mouse female reproductive tracts were collected and straightened by removing the mesosalpinx. The straightened oviduct was fixed with DMSO (Dimethyl sulfoxide, Sigma Aldrich D8418): methanol in the ratio 1:4 and cut into three to four pieces prior to placing at −20°C overnight. The antibody staining protocol was as described in [41]. Blocking was done overnight in solution containing 1% Triton X-100 (Sigma-Aldrich, T8787), 2% powdered milk, and 1× phosphate-buffered saline (PBS, BioShop Canada Inc., PBS405), henceforth referred to as PBSMT. Primary and secondary antibody staining was performed in PBSMT for 5 and 2 days, respectively, at 4° on a shaker. After six 30 min long PBSMT washes, the oviduct pieces were transferred successively to methanol:PBT (1:1, PBT: 1× PBS and 1% Triton X-100), 100% methanol (BioShop Canada Inc., MET302.1), 3% H_2O_2 (BioShop Canada Inc., HYP001.1), and 100% methanol prior to benzyl alcohol/benzyl benzoate (BABB) clearing. BABB-cleared samples were placed on a #1.5 coverslip (Fisher Scientific, 12-545F) with 10–15 μl BABB prior to imaging using the 10× objective (numerical aperture 0.30) on LSM 800 or 710 (Zeiss). Section interval for 3D confocal imaging was 4.32 μm. Usually, 40–110 optical sections were taken.

The fixation and clearing methods used for 3D confocal imaging are known to cause dehydration and tissue shrinkage [42]; thus, we confirmed our findings using 4% paraformaldehyde-fixed open-book preparations, 80% TDE-cleared (2,2'-Thiodiethanol, Sigma-Aldrich, 88559) oviducts, and 2D cryo/paraffin sections. When possible, we imaged live oviducts and open-book preparations dissected from various transgenic mice.

Antibodies

Primary antibodies (1/250 dilution): anti-PAX8 (Proteintech, 10336-1-AP), anti-GFP (Abcam, ab13970), anti-mCherry (Abcam, ab213511), anti-WT1 (Abcam, ab89901), anti-acetylated tubulin (labeled as AT, Sigma, T7451), anti-Sox17 (R&D, AF1924), anti-FoxA2 (Cell Signaling, 3143), and anti-E-cadherin (Invitrogen, 13-1900). Secondary antibodies (1/450 dilution): Alexa Fluor (AF) anti-rabbit 555 (Invitrogen, A31572), AF anti-rabbit 649 (Invitrogen, A21245), AF anti-rabbit 488 (Invitrogen, A21206), AF anti-mouse 649 (Invitrogen, A32787), AF anti-mouse 488 (Invitrogen, A21202), AF anti-goat 568 (Invitrogen, A11057), AF anti-rat 488 (Invitrogen, A21208), anti-chicken 488 (Sigma, SAB4600031), DAPI (4′,6-diamidino-2-phenylindole, Thermo Fisher, 62248)/Hoescht 33342 (Thermo Fisher, 62249), AF 488 phalloidin (Lifetech, A12379), and AF 635 phalloidin (Lifetech, A34054).

Trypan blue injection into the mouse oviduct

Estrus stage and pseudo-pregnant females were anesthetized. The female reproductive tract was exposed either dorsally or ventrally. Under a dissection microscope, filtered trypan blue solution (STEMCELL Technologies, #07050) was injected into the swollen AMP or the ISM using a glass needle. Mice were euthanized; the reproductive tracts were dissected out and straightened slightly.

Image analysis, cell counts, and statistics

3D confocal images were stitched using ImarisStitcher and visualized using FIJI and Imaris. 3D rendering was performed using surfaces function and distance transformation (outside a surface object) MATLAB XTension, followed by manual background removal on Imaris. For optical projections, Maximum/Average/Sum Slices projection in FIJI was used. In some images of Figure 2, PAX8 immunostaining and FLTP-H2B-Venus were overlaid with a single color (cyan) to visualize the epithelial layer in the oviduct, indicated as Epithelium.

2D sections were visualized using FIJI and Zen. Measurements and epithelial cell counting for straightened mouse oviducts were performed manually on FIJI using only transverse 2D sections. Unpaired, two-tailed *t*-test was performed to gauge significance only between successive distal and proximal regions (INF versus AMP, AMP versus distal AIJ, distal AIJ versus proximal AIJ, proximal AIJ versus distal ISM, distal ISM versus proximal ISM, and proximal ISM versus UTJ). For marmoset FT 2D sections, cell counting was performed manually on either transverse or longitudinal sections, with AT and DAPI staining.

Supplementary material

Supplementary material is available at *BIOLRE* online

Acknowledgments

The authors thank the Rosalind and Morris Goodman Cancer Research Centre Histology, the McGill Advanced Bioimaging Facility, and the McGill Integrated Core of Animal Modeling for technical support. The authors thank Dr. Maxime Bouchard for the *Pax2-GFP* mouse line. The authors also thank Drs Keith Murai and Jim Gourdon for marmoset necropsy specimens.

Conflict of interest

The authors declare that they have no conflict of interest.

Authors' contributions

KH executed/analyzed most experiments and wrote/edited the manuscript. MJF, KT, NY, and BY performed some experiments. IB and HL generated mouse lines used and shared unpublished information. MJF, KT, NY, IB, and HL edited the manuscript. YY conceived the project and wrote/edited the manuscript.

References

1. Kölle S, Hughes B, Steele H. Early embryo-maternal communication in the oviduct: A review. *Mol Reprod Dev* 2020; **87**:650–662.
2. Moore EL, Wang S, Larina IV. Staging mouse preimplantation development in vivo using optical coherence microscopy. *J Biophotonics* 2019; **12**:167–182.
3. Prasad SV, Skinner SM, Carino C, Wang N, Cartwright J, Dunbar BS, Williams Z. Structure and function of the proteins of the mammalian zona pellucida. *Cells Tissues Organs* 1999; **285**:251–258.
4. Barton BE, Herrera GG, Anamthathmakula P, Rock JK, Willie AM, Harris EA, Takemaru K, Winuthayanon W. Roles of steroid hormones in oviductal function. *Reproduction* 2020; **159**:R125–R137.
5. Li S, Winuthayanon W. Oviduct: Roles in fertilization and early embryo development. *J Endocrinol* 2017; **232**:R1–R26.
6. Winuthayanon W, Bernhardt ML, Padilla-Banks E, Myers PH, Edin ML, Lih FB, Hewitt SC, Korach KS, Williams CJ. Oviductal estrogen receptor α signaling prevents protease-mediated embryo death. *Elife* 2015; **4**:1–28.
7. Marion LL, Meeks GR. Ectopic pregnancy: History, incidence, epidemiology, and risk factors. *Clin Obstet Gynecol* 2012; **55**:376–386.
8. Briceag I, Costache A, Purcarea VL, Cergan R, Dumitru M, Briceag I, Sajin M, Ispas AT. Fallopian tubes–literature review of anatomy and etiology in female infertility. *J Med Life* 2015; **8**:129–131.
9. Agduhr E. Studies on the structure and development of the bursa ovarica and the tuba uterina in the mouse. *Acta Zool* 1927; **8**:1–133.
10. Dirksen ER, Satir P. Ciliary activity in the mouse oviduct. *Tissue Cell* 1972; **4**:389–403.
11. Stewart CA, Behringer RR. Mouse oviduct development. In: Kubiak J. (eds) Mouse Development. Results and Problems in Cell Differentiation. Berlin, Heidelberg: Springer, 2012; **55**:247–262.
12. Ford MJ, Harwalkar K, Pacis AS, Maunsell H, Wang YC, Badescu D, Teng K, Yamanaka N, Bouchard M, Yamanaka Y. Oviduct epithelial cells constitute two developmentally distinct lineages that are spatially separated along the distal-proximal axis. *bioRxiv Preprint* 2020.
13. Dixon RE, Hwang SJ, Hennig GW, Ramsey KH, Schripsema JH, Sanders KM, Ward SM. Chlamydia infection causes loss of pacemaker cells and inhibits oocyte transport in the mouse oviduct 1. *Biol Reprod* 2009; **80**:665–673.
14. Muro Y, Hasuwa H, Isotani A, Miyata H, Yamagata K, Ikawa M, Yanagimachi R, Okabe M. Behavior of mouse spermatozoa in the female reproductive tract from soon after mating to the beginning of fertilization. *Biol Reprod* 2016; **94**:1–7.
15. Gegg M, Bottcher A, Burtscher I, Hasenoeder S, Campenhout CV, Aichler M, Walch A, Grant SGN, Lickert H. Flattop regulates basal body docking and positioning in mono- and multiciliated cells. *Elife* 2014; **3**:1–24.
16. La Spina FA, Molina LCP, Romarowski A, Vitale AM, Falzone TL, Krapf D, Hirohashi N, Buffone MG. Mouse sperm begin to undergo acrosomal exocytosis in the upper isthmus of the oviduct. *Dev Biol* 2016; **411**:172–182.
17. Suarez SS. Sperm Transport and Motility in the Mouse Oviduct: Observations in situ. *Biol Reprod* 1987; **36**:203–210.
18. Hirate Y, Suzuki H, Kawasumi M, Takase HM, Igarashi H, Kanai Y, Kanai-Azuma M. Mouse Sox 17 haploinsufficiency leads to female subfertility due to impaired implantation. *Sci Rep* 2016; **6**:2–10.
19. Spencer TE, Pru CA, Kelleher AM, DeMayo FJ, Peng W, Pru JK. Forkhead box a2 (FOXA2) is essential for uterine function and fertility. *Proc Natl Acad Sci* 2017; **114**:E1018–E1026.
20. Okano H, Hikishima K, Iriki A, Sasaki E. The common marmoset as a novel animal model system for biomedical and neuroscience research applications. *Semin Fetal Neonatal Med* 2012; **17**:336–340.
21. Cui KH, Matthews CD. Anatomy of adult female common marmoset (Callithrix jacchus) reproductive system. *J Anat* 1994; **185**:481–486.
22. Pfeffer PL, Payer B, Reim G, di Magliano MP, Busslinger M. The activation and maintenance of Pax2 expression at the mid-hindbrain boundary is controlled by separate enhancers. *Development* 2002; **129**:307–318.
23. Avilés M, Coy P, Rizos D. The oviduct: A key organ for the success of early reproductive events. *Anim Front* 2015; **5**:25–31.
24. Talbot P, Geiske C, Knoll M. Oocyte pickup by the mammalian oviduct. *Mol Biol Cell* 1999; **10**:5–8.
25. Lefebvre R, Chenoweth PJ, Drost M, LeClear CT, Mac Cubbin M, Dutton JT, Suarez SS. Characterization of the oviductal sperm reservoir in cattle. *Biol Reprod* 1995; **53**:1066–1074.
26. Maillo V, Sanchez-Calabuig MJ, Lopera-Vasquez R, Hamdi M, Gutierrez-Adan A, Lonergan P, Rizos D. Oviductal response to gametes and early embryos in mammals. *Reproduction* 2016; **152**:R127–R141.
27. Sasanami T, Matsuzaki M, Mizushima S, Hiyama G. Sperm storage in the female reproductive tract in birds. *J Reprod Dev* 2013; **59**:334–338.
28. Suarez SS. Formation of a reservoir of sperm in the oviduct. *Reprod Domest Anim* 2002; **37**:140–143.
29. Suarez SS. Carbohydrate-mediated formation of the oviductal sperm reservoir in mammals. *Cells Tissues Organs* 2001; **168**:105–112.
30. Suarez SS. Interactions of gametes with the female reproductive tract. *Cell Tissue Res* 2016; **363**:185–194.
31. Abe H. The mammalian oviductal epithelium: Regional variations in cytological and functional aspects of the oviductal secretory cells. *Histol Histopathol* 1996; **11**:743–768.
32. Abe H, Oikawa T. Regional differences in the ultrastructural features of secretory cells in the golden hamster (Mesocricetus auratus) oviductal epithelium. *J Anat* 1991; **175**:147–158.
33. Lauschová I. Influence of estrogen and progesterone on ultrastructural indices of oviductal epithelium in sexually immature mice. *Acta Vet* 1999; **68**:13–21.
34. Lauschová I. Secretory cells and morphological manifestation of secretion in the mouse oviduct. *Scripta Medica* 2003; **76**:203–214.
35. Murray MK. Morphological features of epithelial cells in the sheep isthmus oviduct during early pregnancy. *Anat Rec* 1997; **247**:368–378.
36. Ghersevich S, Massa E, Zumoffen C. Oviductal secretion and gamete interaction. *Reproduction* 2015; **149**:R1–R14.
37. Burton JC, Wang S, Stewart CA, Behringer RR, Larina IV. High-resolution three-dimensional in vivo imaging of mouse oviduct using optical coherence tomography. *Biomed Opt Express* 2015; **6**:2713.
38. Burtscher I, Barkey W, Lickert H. Foxa 2-venus fusion reporter mouse line allows live-cell analysis of endoderm-derived organ formation. *Genesis* 2013; **51**:596–604.
39. Burtscher I, Barkey W, Schwarzfischer M, Theis FJ, Lickert H. The Sox17-mCherry fusion mouse line allows visualization of endoderm and vascular endothelial development. *Genesis* 2012; **50**:496–505.
40. McLean AC, Valenzuela N, Fai S, Bennett SAL. Performing vaginal lavage, crystal violet staining, and vaginal cytological evaluation for mouse estrous cycle staging identification. *J Vis Exp* 2012; **67**:4–9.
41. Arora R, Fries A, Oelerich K, Marchuk K, Sabeur K, Giudice LC, Laird DJ. Insights from imaging the implanting embryo and the uterine environment in three dimensions. *Development* 2016; **143**:4749–4754.
42. Azaripour A, Lagerweij T, Scharfbillig C, Jadczak AE, Willershausen B, Van Noorden CJF. A survey of clearing techniques for 3D imaging of tissues with special reference to connective tissue. *Prog Histochem Cytochem* 2016; **51**:9–23.